



Article

Friction Stir Welding of Ti-6Al-4V Using a Liquid-Cooled Nickel Superalloy Tool

Sergei Tarasov , Alihan Amirov , Andrey Chumaevskiy *, Nikolay Savchenko , Valery E. Rubtsov , Aleksey Ivanov, Evgeniy Moskvichev and Evgeniy Kolubaev

Institute of Strength Physics and Materials Science, Siberian Branch of Russian Academy of Sciences, 634055 Tomsk, Russia

* Correspondence: tch7av@ispms.com; Tel.: +7-(3822)-28-68-63

Abstract: Friction stir welding (FSW) of titanium alloy was carried out using liquid cooling of the FSW tool made of heat-resistant nickel superalloy. Cooling of the nickel superalloy tool was performed by means of circulating water inside the tool. The FSW joints were characterized by microstructures and mechanical strength. The mechanical strength of the joints was higher than that of the base metal.

Keywords: friction stir welding; titanium alloys; weld strength; microhardness; X-ray structure analysis; fractography; tool wear



Citation: Tarasov, S.; Amirov, A.; Chumaevskiy, A.; Savchenko, N.; Rubtsov, V.E.; Ivanov, A.; Moskvichev, E.; Kolubaev, E. Friction Stir Welding of Ti-6Al-4V Using a Liquid-Cooled Nickel Superalloy Tool. *Technologies* **2022**, *10*, 118. <https://doi.org/10.3390/technologies10060118>

Academic Editors: Manoj Gupta, Eugene Wong and Gwanggil Jeon

Received: 31 August 2022

Accepted: 17 November 2022

Published: 18 November 2022

Publisher's Note: MDPI stays neutral with regard to jurisdictional claims in published maps and institutional affiliations.



Copyright: © 2022 by the authors. Licensee MDPI, Basel, Switzerland. This article is an open access article distributed under the terms and conditions of the Creative Commons Attribution (CC BY) license (<https://creativecommons.org/licenses/by/4.0/>).

1. Introduction

Titanium alloys are known for having a number of important functional characteristics that include, among others, high corrosion resistance, high specific strength, and biological compatibility [1–3]. Therefore, these alloys are widely used in aerospace, power, and chemical industries, as well as in shipbuilding and surgery [4–6]. Depending on the dominating phase state, titanium alloys can be classified into: α -Ti alloys, which include technical purity grade titanium and titanium alloyed with α -Ti supporting elements; ($\alpha + \beta$)-Ti alloys, containing both α -Ti and β -Ti supporting elements; and β -Ti alloys containing up to 30 wt.% of the β -Ti supporting elements [7,8]. The phase composition of the alloy determines its mechanical characteristics so that ductile alloys contain more β -Ti, while α -Ti attains more strength [9,10].

When it comes to obtaining fusion-welded joints on the titanium alloys, some problems may occur such as overheating, excess grain growth, and high residual stresses due to low heat conductivity [11]. Solutions to these problems may be found when applying thermal post-treatment or/and surface impact treatment [12–14]. An alternative solution may be using friction stir welding (FSW), which has been widely and successfully used for building welded structures from aluminum alloys in aerospace, transportation, and power industries, and the advantage of which is that the joining is by intermixing the solid plasticized and refined metal [15–20].

Earlier experiments with the FSW on titanium alloys have revealed a number of problems, among which the fast wear of the FSW tool and intermixing the wear particles into the weld joint were the most prominent. The most popular materials for fabricating the FSW tools intended for titanium alloys are those with refractory metals, such as tungsten. However, cemented tungsten carbide tools demonstrated high wear despite their good heat resistance [21]. The most stable against wear in FSP (friction stir processing) were the tools made of tungsten-rhenium alloys, though production costs were too high [22]. Polycrystalline cubic boron carbide showed promising results in FSW on steels [23], but was unstable on titanium alloys, as it reacted with titanium, and formed brittle titanium borides and nitrides that were detrimental for the welded joint strength [24,25].

High heat resistance is the main characteristic to provide acceptable wear resistance of the FSW tool, and therefore, one of the possible solutions may be to use nickel superalloys,

which usually work at 900–1000 °C as turbine blades [26]. Such an approach has already been used for friction stir processing on titanium alloys [27]. For example, acceptable results were obtained on technically pure titanium and α' -Ti alloys [28,29]. The wear rate of nickel superalloy tools was also quite high [30] and required some measures to reduce it. Poor heat conductivity may lead to overheating of the tool, loss of strength, as well as enhancing the reaction-diffusion between the tool and the stirred alloy. The natural remedy may be cooling the tool by means of fluid flow.

This work was focused on studying the effect of the FSW nickel superalloy tool cooling on the FSW tool wear, FSW joint characteristics and microstructures of the FSW joint zones.

2. Materials and Methods

2.1. Experimental Set-Up and Materials

The FSW on a Ti-6Al-4V was carried out with the use of argon blow shielding against oxidizing the seam metal. Argon was supplied via an inlet directly to the welding zone, as shown in Figure 1. Titanium alloy sheets with 2.5 mm thickness were secured on an AISI 304 stainless steel substrate using special clamps. On plunging the tool into the metal, the plunging force was maintained at the constant level. The tool inclination with respect to the horizontal plane was 1.5°. A liquid flow cooling system was used to supply a coolant via an axial hole, and thus, limit the tool's heating (Figure 2).

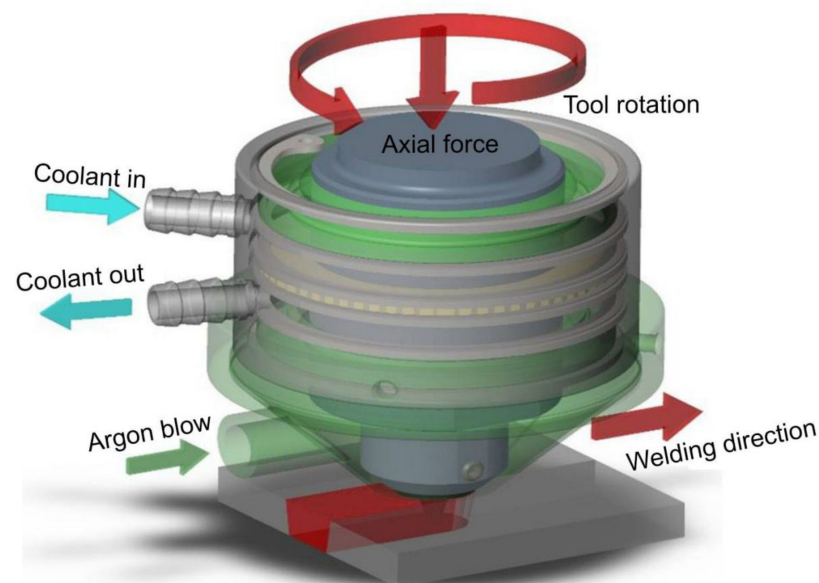


Figure 1. Schemes of friction stir welding titanium alloys with argon gas blanket of the welding joint and liquid tool cooling. Blue and green arrows show the coolant fluid and gas flow directions, respectively. Red arrows show the tool rotation and transverse motion and axial plunging force. Directions.

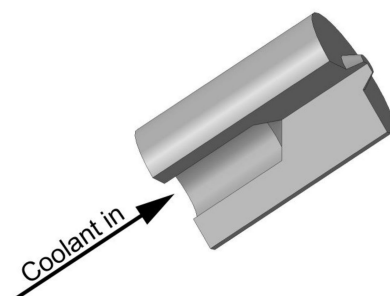


Figure 2. Scheme of working tool from ZhS6U alloy for FSW titanium alloys. The arrow shows the coolant inflow direction.

The tool's shoulder and pin diameters were 20 mm and 3 mm, respectively, with the pin's height at 2.3 mm. The compositions of nickel superalloy and titanium alloys are shown in Tables 1 and 2.

Table 1. Element composition of ZhS6U superalloy (wt%).

Fe	Nb	Ti	Cr	Co	W	Ni	Al	Mo	C
≤1	0.8–1.2	2–2.9	8–9.5	9–10.5	9.5–11	54.3–62.7	5.1–6	1.2–2.4	0.13–0.2
Ce	Si	Mn	P	S	Zr	Bi	B	Y	Pb
≤0.02	≤0.4	≤0.4	≤0.015	≤0.01	≤0.04	≤0.0005	≤0.035	≤0.01	≤0.01

Table 2. Element composition of Ti-6Al-4V alloy (wt%).

Fe	C	Si	V	N	Ti	Al	Zr	O	H	Other
≤0.6	≤0.1	≤0.1	3.5–5.3	≤0.05	86.45–90.9	5.3–6.8	≤0.3	≤0.2	≤0.015	0.3

The FSW was initially performed with parameters as reported elsewhere [31], but later, their values were corrected for a new tool design and were as follows: axial force in plunging and welding were $F_p = 43$ kN and $F_w = 45$ kN, respectively; welding speed $V = 86$ mm/min; rotation rates $n_1 = 340$, $n_2 = 360$, and $n_3 = 380$ RPM for samples 1, 2, and 3, respectively.

2.2. Equipment and Sample Preparation

The metallographic views were prepared by cutting the joint in a plane perpendicular to the welding direction, then grinding and polishing the section on abrasive papers with grain sizes P180 to P2000 and diamond paste ACM 1/0. Etching was carried out in a reagent composed of $C_3H_8O_3$ —30 mL, HNO_3 —10 mL, and HF —10 mL, for 30–35 s.

Microstructural examination was performed using an optical microscope «Altami Met 1S». An SEM field emission cathode instrument FEG SEM Apreo 2 S (Thermo Fisher Scientific, Waltham, MA, USA) attached to an EDS Octane Elect Super (EDAX) analyzer was used for fractography.

An XRD diffractometer DRON 7 operated at 36 kV, 22 mA, $CoK\alpha$ radiation with wavelength 1.7902 Å, diffraction angle 2θ interval 15–102°, with 0.05° step, and exposition of 40 s was used to characterize phases formed. A symmetrical Bragg–Brentano XRD configuration ($\theta/2\theta$) was applied for identifying phases formed in basic Ti-6Al-4V alloy, basic nickel superalloy, and in the welded joints. Grazing-incidence X-ray diffraction was used to detect phases on the worn surfaces of the nickel superalloy at a beam incidence angle of 13°.

The XRD peak identification was performed using Crystal Impact's "Match!" software version 3.9 (Crystal Impact, Bonn, Germany). The relative peak intensities of α -Ti and β -Ti phases $R(x)$, were calculated from Formula (1) as follows [32]:

$$R(x) = (I(x)/\sum I(A)) \times 100 \quad (1)$$

where $I(x)$ is the intensity of the 'x' phase reflection; $\sum I(A)$ is the sum of all reflection intensities.

A microhardness tester «Affairs DM8» at 100 g load and a dwell time 10 s allowed for the obtaining of microhardness numbers at 1 mm steps along the lines 11 mm away from the centerline. Tensile tests were carried out using a tensile machine UTS 110M-100 at room temperatures on samples cut off the welded joints, as shown in Figure 3.

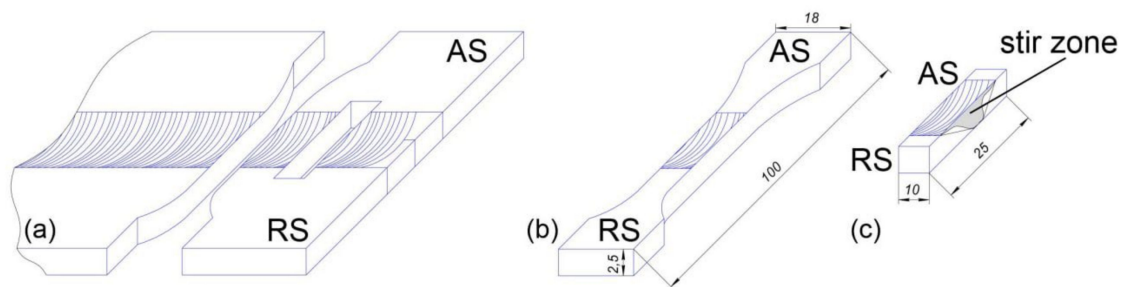


Figure 3. Scheme of the FSW seam sectioning (a) for cutting off tensile (b) and metallographic (c) specimens. AS and RS are the advancing and retreating sides of the seam, respectively.

3. Results

The as-received Ti-6Al-4V alloy and nickel superalloy are represented by 73% vol. of α -Ti + 27 vol.% of β -Ti (Figure 4a) and $\gamma(\gamma')$ + MC carbides (Figure 4b), respectively.

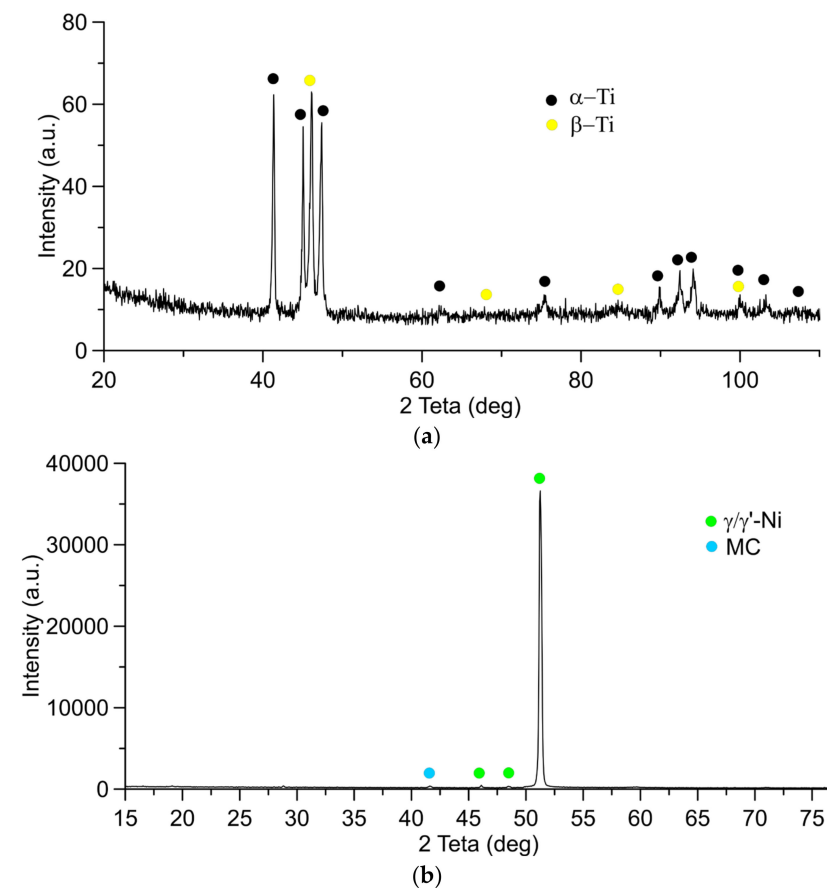


Figure 4. The X-ray diffraction patterns of the basic Ti-6Al-4V alloy (a) and nickel superalloy (b).

According to the XRD pattern in Figure 5a, the welded joint metal contains both these phases, but this time the β -Ti content decreased to 16 vol.% because of the phase transformations in heating and cooling [33]. More dramatic changes occurred to the FSW tool surface, which has been covered by a tribological layer where intermetallic compound (IMC) Ti_2Ni and carbides, such as MC, M_2C , and M_3C_2 , are detected using the grazing-incidence X-ray diffraction; here, M stands for W, Cr, Nb (Figure 5b).

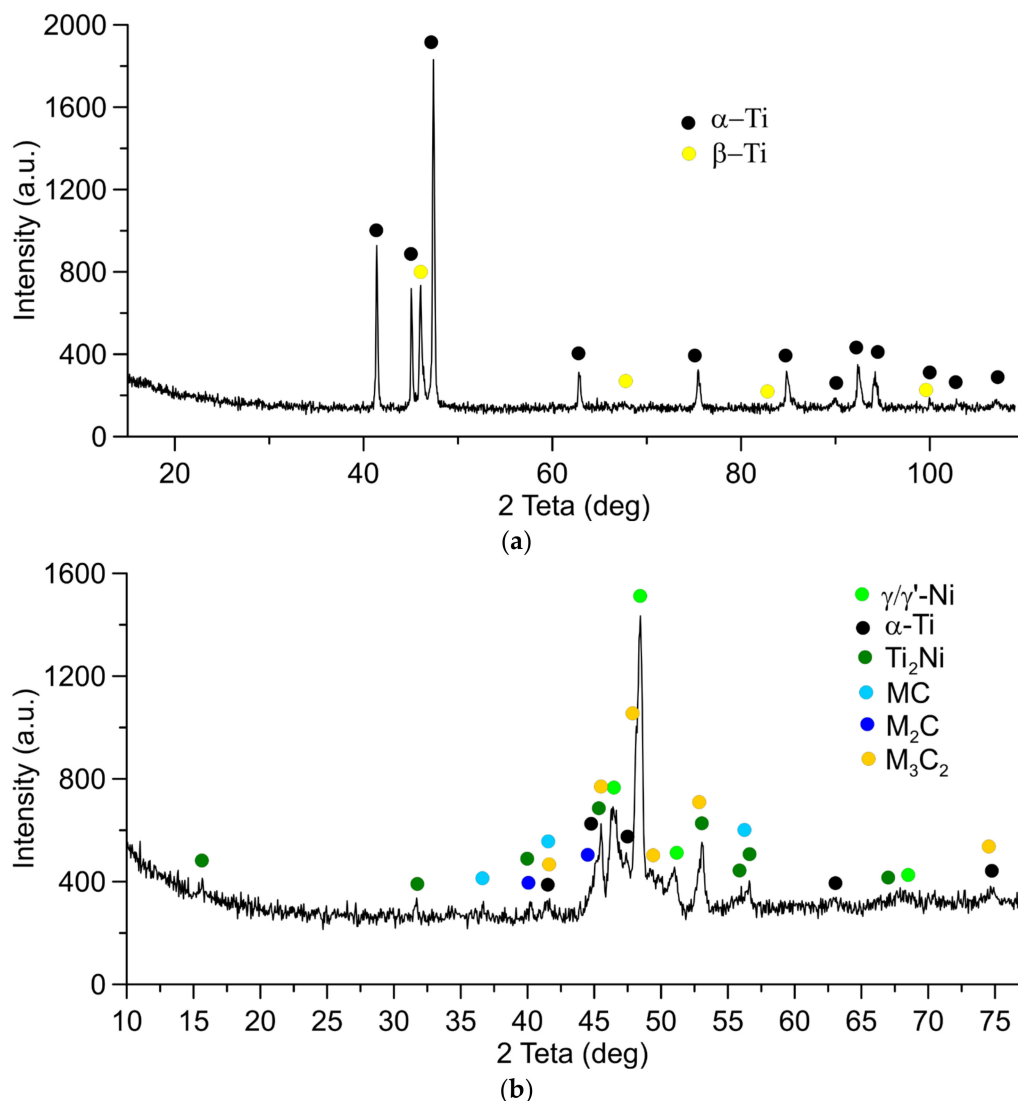


Figure 5. The X-ray diffraction patterns from the stir zone on the welded titanium alloy (a) and tribological layer on the corresponding FSW tool shoulder surface (b).

In general, the macrostructures typical of the FSW joints [34] can be observed on the optical cross-section views in Figures 6–8 and with some specificity stemming from the poor heat conductivity and high strength of the titanium alloy. Such a specificity mainly relates to forming a narrow heat-affected zone (HAZ) [35,36] and absence of a thermomechanically affected zone (TMAZ) [36–39]. A wormhole defect can be observed in a joint obtained according to regime 1 with the lowest rotation rate (Figure 8). No wormholes were detected in the samples welded according to regimes 2 and 3 with the increased rotation rates.

All samples demonstrate some specific branching structures located closer to the bottom part of the stir zone. It has been shown previously [25,27] that these structures are formed by intermixing the tool's wear particles with the SZ metal. The higher the rotation rate, the higher the temperature and more titanium alloy is transferred on the tool's surface, where reaction diffusion between titanium and nickel occurs with ensuing formation of intermetallic compounds (IMC) and wear particles, which then intermix with the metal welded. This coarse wear particle can be observed in sample 3, with the SZ obtained at the highest rotation rate (Figure 8).

The microstructure (Figure 9) of the as-received base metal is characterized by α -Ti and β -Ti grains of mean sizes $4.1 \pm 1.5 \mu\text{m}$ and $1.2 \pm 0.3 \mu\text{m}$, respectively. The SZ metal is represented by recrystallized α -Ti $0.53 \pm 0.2 \mu\text{m}$ grains; i.e. at least 87% grain refining

effect was achieved that resulted in the increased ultimate tensile strength and reduced plasticity of the SZ metal by grain boundary hardening mechanism.

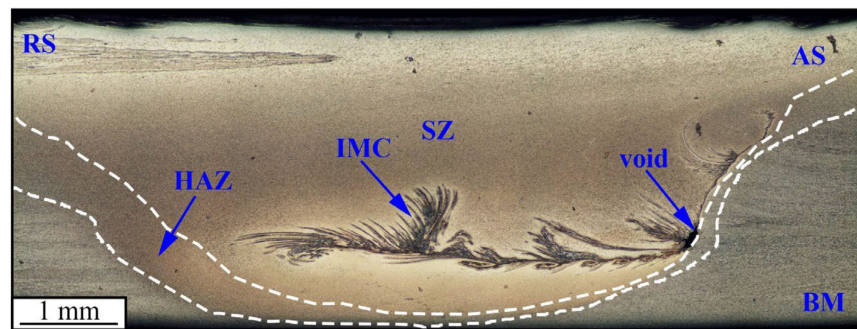


Figure 6. Cross-sectional metallographic image of specimen No. 1.

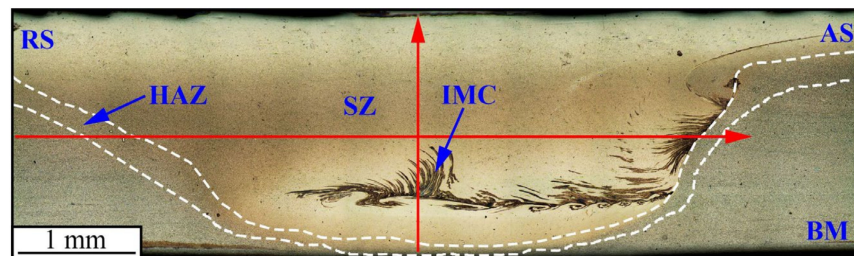


Figure 7. Cross-sectional metallographic image of specimen 2. Red lines identify the lines of microhardness profiles.

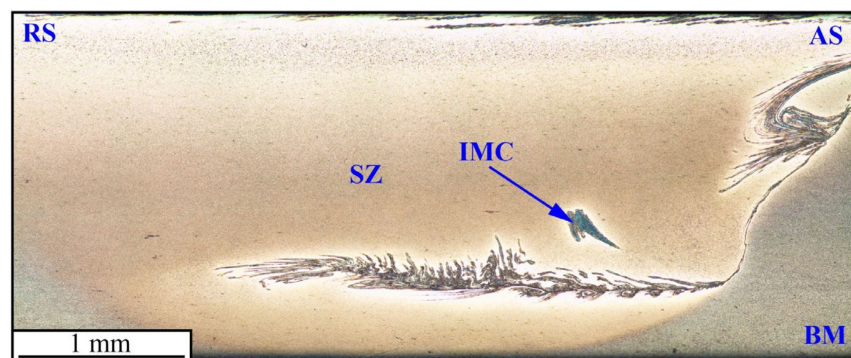


Figure 8. The stir zone image of specimen 3.

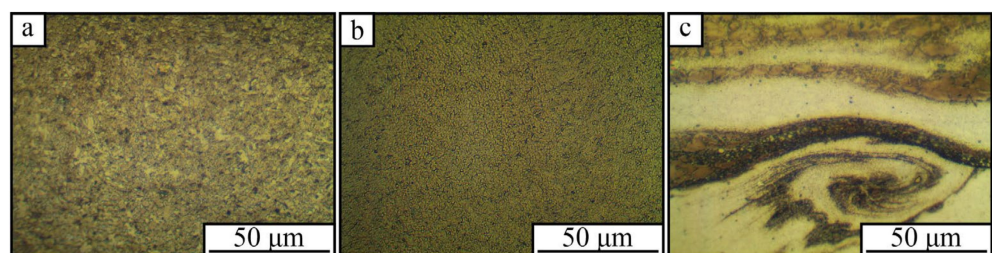


Figure 9. Microstructure of Ti-6Al-4V alloy in the base metal (a), SZ (b), and IMC in SZ (c).

The IMC zones intermixed with the IMC-free areas are represented in more detail in Figure 10a,b. Figure 10b denotes the EDS probe zones with compositions shown below in Table 3. The dark areas in Figure 10 (Table 3, pos. 8–13) contain elements inherent to the

Ti-6Al-4V alloy, while areas with the light-gray particles additionally contain Cr, Co, Ni, and W; i.e., elements that initially belonged to the tool alloy.

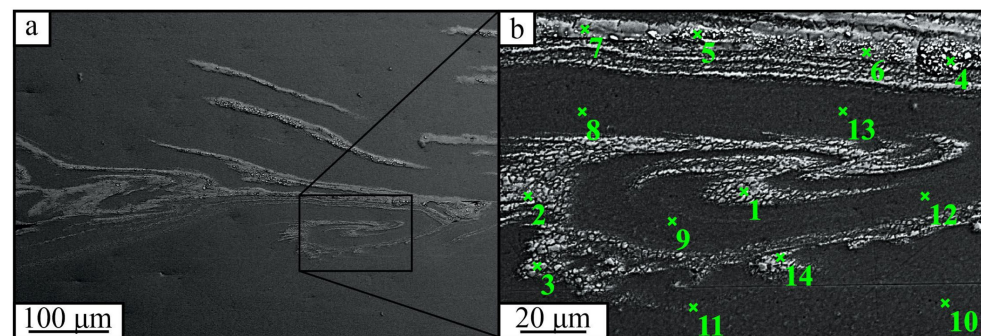


Figure 10. SEM image the IMCs intermixed with the stir zone (a) and enlarged view of these IMC structures with the EDS probe zones numbered from 1 to 14 (b), whose EDS spectra are identified in Table 3 below.

Table 3. The EDS element compositions of the FSW TiAl64V stir zone in points as shown in Figure 10.

Spectrum	Chemical Element Content, Atomic/Weight %						
	Al	Ti	V	Cr	Co	Ni	W
1	9.91/5.68	79.35/80.71	3.48/3.76	1.13/1.24	0.92/1.16	4.85/6.05	0.36/1.40
2	9.55/5.50	78.41/80.16	3.56/3.87	1.09/1.21	1.10/1.39	6.28/7.86	-
3	9.93/5.70	80.22/81.79	3.65/3.96	1.00/1.10	0.68/0.85	4.18/5.22	0.35/1.37
4	9.65/5.34	70.04/68.82	3.11/3.25	1.94/2.07	1.75/2.11	12.69/15.28	0.83/3.12
5	8.17/4.55	74.06/73.23	3.07/3.22	1.80/1.93	1.83/2.22	10.53/12.76	0.55/2.08
6	9.97/5.63	74.24/74.40	3.29/3.51	1.31/1.42	1.31/1.62	9.39/11.54	0.49/1.88
7	10.09/5.79	79.23/80.69	3.44/3.72	0.82/0.91	1.04/1.31	5.06/6.31	0.32/1.27
8	9.86/5.79	86.42/90.09	3.72/4.12	-	-	-	-
9	9.72/5.70	86.59/90.20	3.70/4.10	-	-	-	-
10	9.99/5.87	86.14/89.84	3.87/4.29	-	-	-	-
11	10.25/6.03	86.28/90.12	3.47/3.85	-	-	-	-
12	9.77/5.73	86.19/89.79	4.04/4.48	-	-	-	-
13	10.13/5.96	85.95/89.69	3.92/4.35	-	-	-	-
14	10.08/5.79	80.18/81.69	3.43/3.71	0.84/0.93	0.67/0.84	4.41/5.51	0.39/1.53

These areas were characterized by microhardness numbers at the level of 4.40–5.30 GPa, while microhardness of the stirring zone was in the range 3.75–4.05 GPa; i.e., about 20% higher than that of the base metal (Figure 11).

Tensile testing showed that, despite there were regions with intermixed tool wear particles, the joint strength values of all samples were higher than that of the base metal (Figure 12), while the maximum strength was achieved on samples obtained according to regime 3, with fracture occurred outside of the stir zone at a $\sim 45^\circ$ angle and with respect to the tensile axis (Figure 13). Samples 1 and 2 demonstrated fracture localization inside their stir zones closer to the retreating side (RS) and in a normal direction to the tensile axis. These samples had higher strength values than that of the as-received Ti6Al4V, but the lowest strain-to-fracture values. It seems that neither the presence of a void in sample 1 nor the large amount of IMCs formed on the advanced sides (AS) of all samples had any detrimental effect on the sample's tensile strength.

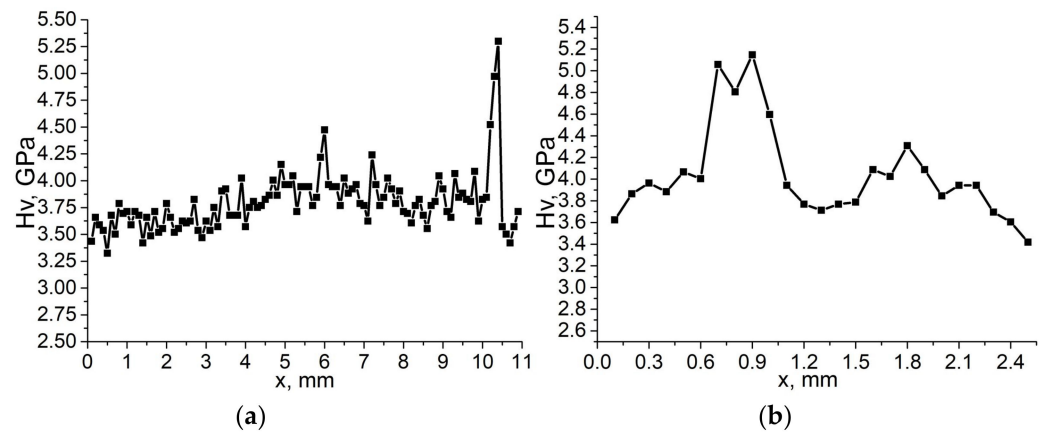


Figure 11. Microhardness of the welded joint Ti-6Al-4V alloy obtained by friction stir welding with nickel-base heat-resistant tool along the green lines shown in Figure 7: (a) vertical profile; (b) horizontal profile.

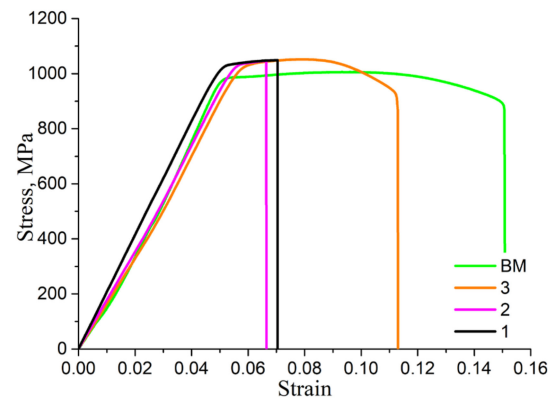


Figure 12. The tensile stress-strain curves obtained on samples 1, 2 and 3 produced with 340, 360 and 380 RPM rotation rates.

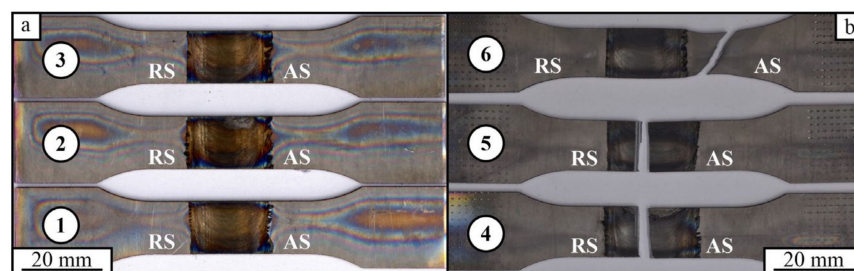


Figure 13. The tensile samples cut off the FSW welds obtained at tool rotation rates 340 (1 and 4), 360 (2 and 5) and 380 (3 and 6) RPM before (a) and after (b) the tensile tests.

The same conclusion may be obtained from the tensile curve of sample 3. Moreover, this time the fracture was localized on the RS outside of the stir zone with intermetallic compounds. This can be interpreted at least as the lack of tensile strength sensitivity to the IMC structures, as well as defects.

The XRD diffractogram obtained from the fracture surface of sample 2 shows the presence of both α -Ti and β -Ti (Figure 14) without any reflections from Ti_2Ni IMCs that were formed on the surface of the superalloy tool and then intermixed with the titanium alloy, thus forming those IMC branched structures, as shown in Figures 6–8.

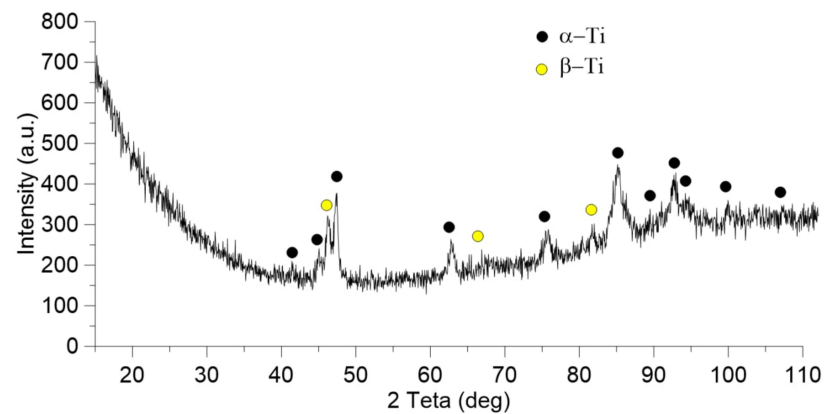


Figure 14. The X-ray diffraction pattern of the weld fracture surface after mechanical testing on the sample 2.

The fracture surfaces SEM SE images obtained from samples 1 and 2 present large bulges, ledges, and dimples, testifying on the development of a crack in inhomogeneous structures (Figure 15a–e). The SEM BSE images (Figure 15b–f), however do not reveal any regions with the BSE contrast, other than that of the titanium alloy, and therefore, are interpreted as nickel-rich IMCs. This result, being combined with the XRD pattern in Figure 14, confirms the absence of IMCs on the fracture surface and at least 15 μm below it, which is the maximum X-ray penetration in a titanium alloy, at $2\Theta = 160^\circ$. Nevertheless, the small scale surface images suggest a viscous type of fracture in the fine-crystalline stir zones. The fracture surface of sample 3 is located outside of the stir zone with some necking (Figure 15b, sample 3), which could also be interpreted in terms of the viscous type of fracture developing through the SZ away from the IMC structures.

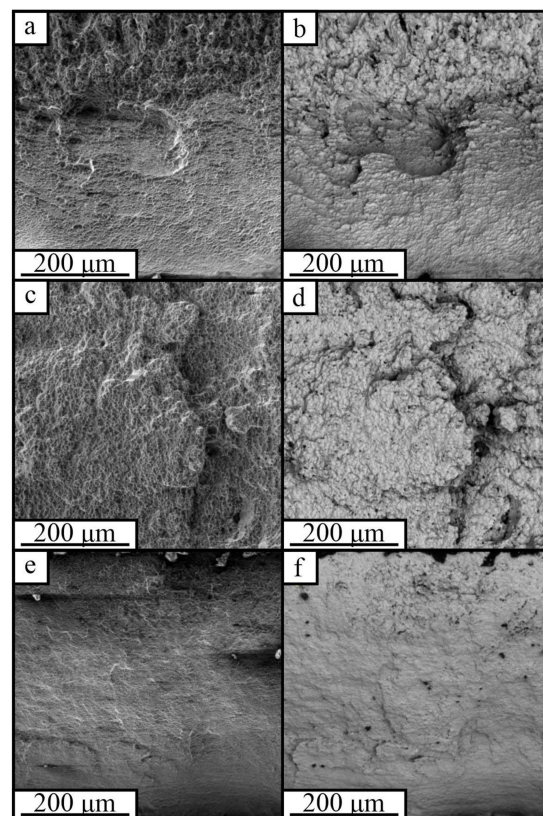


Figure 15. SE/BSE-images of fracture surfaces obtained from sample 1 (a,b), 2 (c,d), and 3 (e,f).

The FSW tool resistance against wear during FSW on the titanium alloys can be evaluated from a comparison between the new and worn tools in Figure 16a,b. The worn tool had a smaller height pin and shoulder surface coated by transferred titanium alloy (Figure 16b). The most intense wear, however, occurred on the pin root surface where an annular groove had formed. The use of water cooling reduced the FSW tool pin wear after welding at least a 2 m long weld seam, while partially retaining the pin shape (Figure 16b,c).

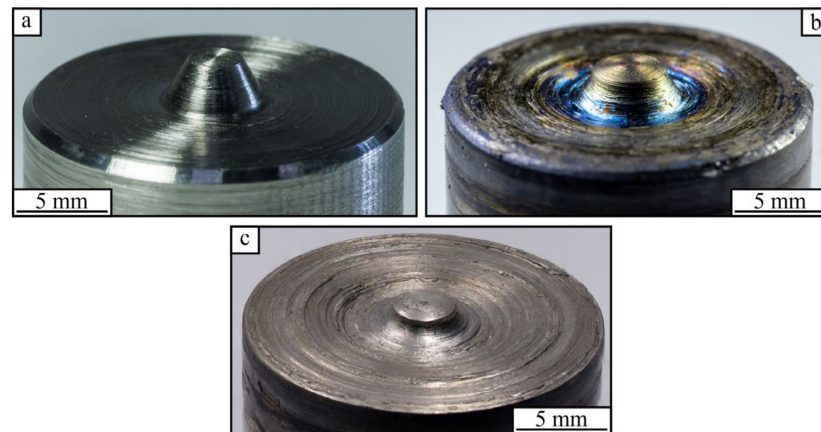


Figure 16. FSW tool produced from alloy ZhS6U before welding (a), after ≈ 2 m of welding (b), and after ≈ 2 m of welding without water cooling (c).

As shown above, the use of a grazing incidence angle XRD allowed identifying IMCs and carbides in the tribological layer that covered the FSW tool shoulder worn surface. However, there were zones on the tool surface that differed morphologically (Figure 17a–c). It has been shown, when studying the FSW tool wear in FSP on Ti-Cu system [27], that the shoulder worn surface revealed the lowest wear rate, generating a thick and anti-wear tribological layer. The same type of layer was generated on the FSW tool's shoulder surface in the present work (Figure 17a). This layer also contained gray Ti_2Ni IMC regions (Figure 17a, pos. 1) and bright carbide particles (Figure 17a, pos. 2). The cross-section view of the FSW tool subsurface allowed observing a rather thick tribological layer that could be structurally divided into an upper transfer layer, almost fully consisting of adhesion transferred Ti (Figure 18a), and a transition layer, composed of Ti_2Ni with a tungsten-based carbide network (Figure 18a, pos 5, 6). The EDS element profiles across the tribological layer confirmed the above suggestions (Figure 19).

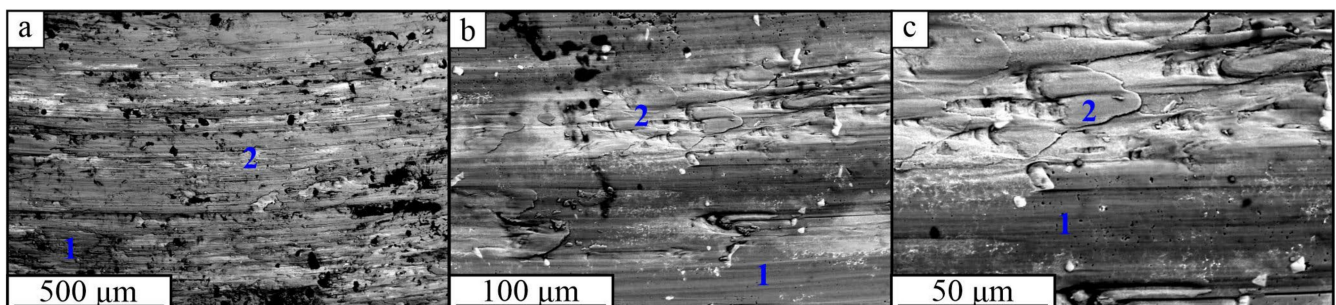


Figure 17. SEM BSE images of the worn surface zones on the FSW tool shoulder (a–c): 1—intermetallic regions, 2—carbides.

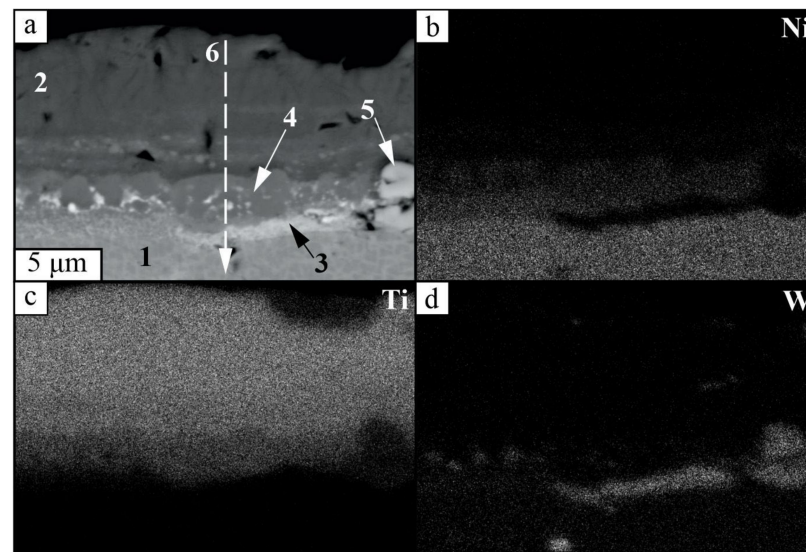


Figure 18. The SEM BSE image of tribological layer structures on the FSW tool worn surface (a) and corresponding EDS element distribution maps (b–d): 1—base superalloy metal; 2—transfer layer, intermetallic compound; 3—fine tungsten carbides; 4—carbide network in the transition layer; 5—large carbide particles; 6 is the EDS probe trajectory.

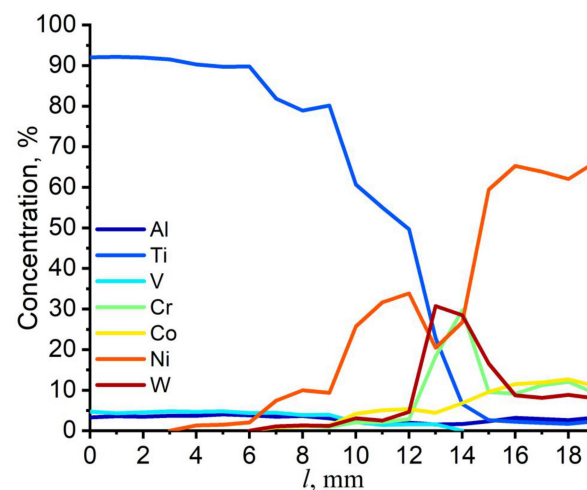


Figure 19. EDS element profiles obtained along trajectory 6 in Figure 18a.

The most intensive wear occurred on the pin/shoulder fillet surface, so that corresponding worn surfaces demonstrated areas deprived of any tribological layer (Figure 20a,c, pos. 1, 2) or tribological layer fragments (Figure 20, pos. 3) with primary carbides (Figure 20b, pos. 4). The cross-section views of pin/shoulder fillet area demonstrated either full absence of the tribological layer (Figure 20d) or the presence of its fragments (Figure 20e, pos. 5) structurally consisting of Ti_2Ni in the Ti matrix. This meant that this area experienced intensive wear with the removal of the tool material. The subsurface superalloy structure carbides could be seen on the worn surface, while no carbide network could be found in the tribological layer fragments (Figure 20e).

The worn surface of the pin end could be characterized by the absence of any tribological layer (Figure 21a) with transfer layer areas (Figure 21b, pos. 2) and concentric wear grooves (Figure 21a,c) with the detached fragments (Figure 21c, pos. 3).

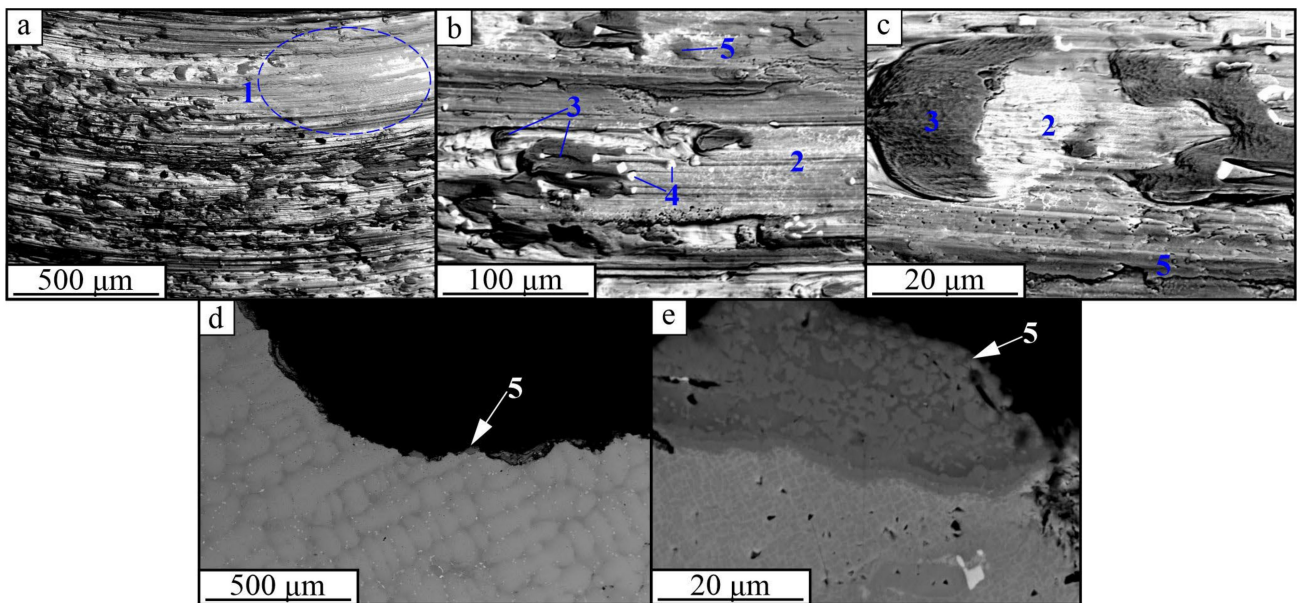


Figure 20. SEM BSE images of subsurface FSW tool structures on the worn surface (a–c) and below the pin/shoulder fillet worn surface without (d) and with tribological layer fragments (e): 1, 2—tribological layer-free regions; 3—transfer layer fragments; 4—primary carbides; 5—intermetallic layer fragments.

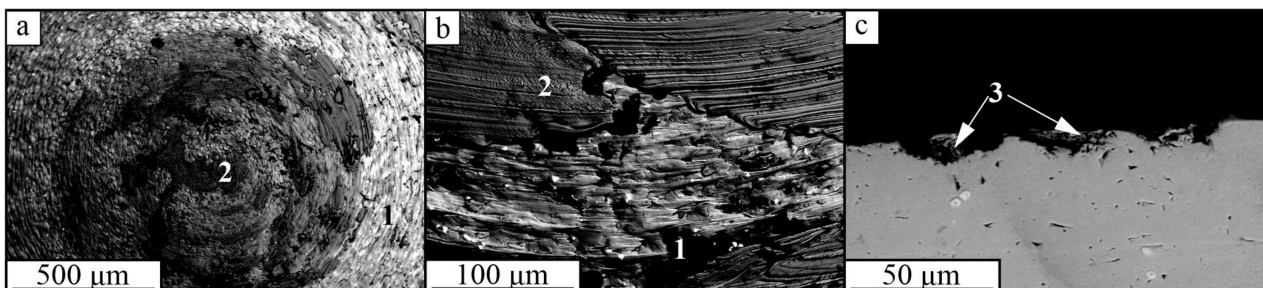


Figure 21. SEM BSE images of the pin end worn surface with transfer layer areas ((a,b), pos. 2) and detached wear debris ((c), pos. 3).

4. Discussion

It was observed that the tensile characteristics of all samples were not sensitive to the IMC structures formed in them by intermixing with wear particles detached from practically consumable FSW tool. Considering the data obtained, the improved strength and loss of ductility of the welded joint, as compared to those of the as-received Ti-6Al-4V (Figure 12), could be caused by at least two reasons. The first and well-known reason could be the SZ strengthening by grain refinement according to the Hall-Petch mechanism. The second reason could be the phase transformation occurred in SZ during cooling. It is known that the dual-phase titanium alloys were developed especially for combining high strength with acceptable ductility, so that increasing the content of β -Ti attains more ductility and less hardening and vice versa; increasing the content of α -Ti corresponds to higher ultimate strength and less ductility [2,12]. Therefore, the higher strength of the welded joints in samples 1 and 2 may be due to reduced content of β -Ti and higher content of α -Ti, as well as extra α' -Ti formed in the welded joint (Figure 5). Heating and stirring in FSW was accompanied by $\alpha + \beta \rightarrow \beta$ transformation, while during cooling there occurred $\beta \rightarrow \alpha' + \alpha + \beta$ [40]. The higher plasticity of sample 3 FSWed at the highest tool rotation rate and, therefore, at higher temperature, could have resulted from slow cooling and forming a higher amount of residual β -Ti as compared to those in samples 1 and 2.

The third reason could be that fine intermetallic compounds, such as Ti_2Ni , may be distributed in the SZ metal and actually serve as reinforcing particles (Figure 11). These types of structures have been observed in SZ of TiAl6V4 friction stir processed and intermixed with copper powder [27]. The nanosized Ti_2Ni precipitates formed on the TiAl6V4 grains and caused a dislocation of the barriers (Figure 22). The same IMC structures were formed in this FSW work. The IMC refining can be an additional factor in the SZ hardening.

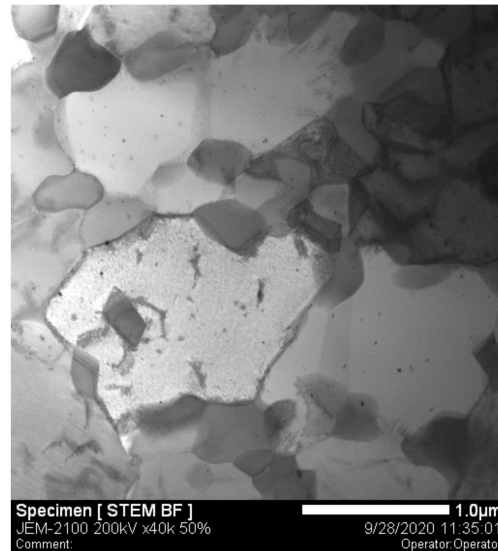


Figure 22. Ti_2Ni grain boundary precipitates in TiAl6V4 + Cu powder after friction stir processing.

The presence of a clearly observable tribological layer on the shoulder surface (Figure 16b) can be taken as a good indication from the point of view of the actual mechanism of degradation of the tool material during welding. It is known that the formation of so-called mechanically mixed layers (MML) is one of the most important aspects of the interaction between the FSW tool and the material being welded [27]. For FSW, these MMLs formed on the tool surface due to the high adhesion of the heated and plasticized Ti6Al4V titanium alloy material. Despite the water-cooling system being applied to avoid overheating of the tool, due to the high temperature reactivity and low thermal conductivity of Ti6Al4V, the diffusion-reaction occurred between the MML and the tool material to form the Ti_2Ni intermetallic compound (Figure 12). At the same time, such a diffusion reaction led to the formation of a continuous protective film, and did not form brittle intermetallic protrusions, outgrowths, spikes, and other similar formations that might contribute to the appearance of stress concentrators, due to which large wear particles would be formed by brittle fracture, and then, accordingly, caused the undesirable abrasive wear. In other words, the improved resistance to thermal degradation was observed in case of using the liquid-cooled nickel superalloy tool for FSW on Ti6Al4V.

Generally, the worn surfaces of the FSW tool used in this welding experiment with cooling can be characterized by the less wear intensity as compared to those reported previously [27]. Such a conclusion mostly relates to the pin end and pin root worn surfaces which demonstrated less deep grooves and adhesion wear traces as those obtained by FSP intermixing of copper powder in TiAl6V4 [27], where intense exothermic diffusion reaction between Ti and Cu occurred that additionally increased the temperature during contact between the tool and alloy.

5. Conclusions

The FSW experiments were conducted using a heat-resistant nickel superalloy tool on a titanium ($\alpha + \beta$)-alloy under conditions of water cooling. Such an approach allowed obtaining a weld joint with a tensile strength higher than that of the base metal (sample 3),

despite the formation of the Ti_2Ni intermetallic compounds on the tool surface and intermixing them with the stirring zone metal in the form of IMC-branched structures. As shown by fractography, these IMC structures were not present on the fracture surfaces of samples after tensile testing, and therefore, did not embrittle the stir zone. The use of a FSW tool water cooling reduced the wear of the FSW tool made of nickel superalloy.

Author Contributions: Conceptualization, A.C. and S.T.; methodology, A.A., A.C. and S.T.; validation, A.A., V.E.R. and A.C.; formal analysis, A.I. and A.A.; investigation, A.A., A.C., N.S. and E.M.; resources, E.K. and V.E.R.; writing—original draft preparation, A.A. and S.T.; writing—review and editing, S.T. and A.C.; visualization, A.I. and A.A.; supervision, S.T.; project administration, S.T. and A.C.; funding acquisition, A.C. and S.T. All authors have read and agreed to the published version of the manuscript.

Funding: This work was performed under the Russian Science Foundation grant No. 22-29-01621.

Institutional Review Board Statement: Not applicable.

Informed Consent Statement: Not applicable.

Data Availability Statement: All data included in the main text.

Acknowledgments: The investigations have been carried out using the equipment of Share Use Centre “Nanotech” of the ISPMS SB RAS.

Conflicts of Interest: The authors declare no conflict of interest.

References

- Pilchak, A.L.; Juhas, M.C.; Williams, J.C. Microstructural Changes Due to Friction Stir Processing of Investment-Cast Ti-6Al-4V. *Met. Mater. Trans. A* **2007**, *38*, 401–408. [[CrossRef](#)]
- Balasundar, I.; Raghu, T.; Kashyap, B.P. Hot working and geometric dynamic recrystallisation behaviour of a near- α titanium alloy with acicular microstructure. *Mater. Sci. Eng. A* **2014**, *600*, 135–144. [[CrossRef](#)]
- Zhu, Y.Y.; Bo, C.H.E.N.; Tang, H.B.; Cheng, X.; Wang, H.M.; Jia, L.I. Influence of heat treatments on microstructure and mechanical properties of laser additive manufacturing Ti-5Al-2Sn-2Zr-4Mo-4Cr titanium alloy. *Trans. Nonferr. Met. Soc. China* **2018**, *28*, 36–46. [[CrossRef](#)]
- Steele, M.C.; Hein, R.A.; He, T.; Chen, W.; Wang, W.; Ren, F.; Stock, H.R. Superconductivity of Titanium. *J. Phys. Rev.* **1953**, *92*, 243–247. [[CrossRef](#)]
- Gorsse, S.; Miracle, D.B. Mechanical properties of Ti-6Al-4V/TiB composites with randomly oriented and aligned TiB reinforcements. *Acta Mater.* **2003**, *51*, 2427–2442. [[CrossRef](#)]
- Qian, T.T.; Dong, L.I.U.; Tian, X.J.; Liu, C.M.; Wang, H.M. Microstructure of TA2/TA15 graded structural material by laser additive manufacturing process. *Trans. Nonferr. Met. Soc. China* **2014**, *24*, 2729–2736. [[CrossRef](#)]
- Jiang, L.; Huang, W.; Liu, C.; Chai, L.; Yang, X.; Xu, Q. Microstructure, texture evolution and mechanical properties of pure Ti by friction stir processing with slow rotation speed. *Mater. Charact.* **2019**, *148*, 1–8. [[CrossRef](#)]
- Mironov, S.; Sato, Y.S.; Kokawa, H. Development of grain structure during friction stir welding of pure titanium. *Acta Mater.* **2009**, *57*, 4519–4528. [[CrossRef](#)]
- Liu, F.C.; Liao, J.; Gao, Y.; Nakata, K. Influence of texture on strain localization in stir zone of friction stir welded titanium. *J. Alloys Compd.* **2015**, *626*, 304–308. [[CrossRef](#)]
- Zhang, W.; Ding, H.; Cai, M.; Yang, W.; Li, J. Ultra-grain refinement and enhanced low-temperature superplasticity in a friction stir-processed Ti-6Al-4V alloy. *Mater. Sci. Eng. A* **2018**, *727*, 90–96. [[CrossRef](#)]
- Junaid, M.; Rahman, K.; Khan, F.; Bakhsh, N.; Baig, M. Comparison of microstructure, mechanical properties, and residual stresses in tungsten inert gas, laser, and electron beam welding of Ti-5Al-2.5 Sn titanium alloy. *Proc. Inst. Mech. Eng. Part L-J. Mater.-Des. Appl.* **2019**, *233*, 1336–1351. [[CrossRef](#)]
- Wang, B.; Yao, X.; Liu, L.; Zhang, X.; Ding, X. Mechanical properties and microstructure in a fine grained Ti-5Al-5Mo-5V-1Cr-1Fe titanium alloy deformed at a high strain rate. *Mater. Sci. Eng. A* **2018**, *736*, 202–208. [[CrossRef](#)]
- Liu, H.; Fujii, H. Microstructural and mechanical properties of a beta-type titanium alloy joint fabricated by friction stir welding. *Mater. Sci. Eng. A* **2018**, *711*, 140–148. [[CrossRef](#)]
- Ashton, P.J.; Jun, T.; Zhang, Z.; Britton, T.B.; Harte, A.M.; Leen, S.B.; Dunne, F.P.E. The effect of the beta phase on the micromechanical response of dual-phase titanium alloys. *Int. J. Fatigue* **2017**, *100*, 377–387. [[CrossRef](#)]
- Kolubaev, E.A.; Luo, A.A. A Distinctions of structure forming of welded joints produced by friction stir welding. *Prog. Mater. Sci.* **2008**, *53*, 980–1023. [[CrossRef](#)]
- Threadgill, P.L. Terminology in friction stir welding. *Sci. Technol. Weld. Join.* **2007**, *12*, 357–360. [[CrossRef](#)]

17. Sato, Y.S.; Park, S.H.C.; Matsunaga, A.; Honda, A.; Kokawa, H. Novel production for highly formable Mg alloy plate. *J. Mater. Sci.* **2005**, *40*, 637–642. [[CrossRef](#)]
18. Li, G.; Zhou, L.; Luo, S.; Dong, F.; Guo, N. Microstructure and mechanical properties of bobbin tool friction stir welded ZK60 magnesium alloy. *Mater. Sci. Eng. A* **2020**, *776*, 138953. [[CrossRef](#)]
19. Kulkarni, S.S.; Truster, T.; Das, H.; Gupta, V.; Soulami, A.; Upadhyay, P.; Herling, D. Microstructure-Based Modeling of Friction Stir Welded Joint of Dissimilar Metals Using Crystal Plasticity. *J. Manuf. Sci. Eng.* **2021**, *143*, 121008. [[CrossRef](#)]
20. Kulkarni, S.S.; Gupta, V.; Ortiz, A.; Das, H.; Upadhyay, P.; Barker, E.; Herling, D. Determining cohesive parameters for modeling interfacial fracture in dissimilar-metal friction stir welded joints. *Int. J. Solids Struct.* **2021**, *216*, 200–210. [[CrossRef](#)]
21. Rai, R.; De, A.; Bhadeshia, H.K.D.H.; DebRoy, T. Review: Friction stir welding tools. *Sci. Technol. Weld. Join.* **2011**, *16*, 325–342. [[CrossRef](#)]
22. Farias, A.; Batalha, G.F.; Prados, E.F.; Magnabosco, R.; Delijaicov, S. Tool wear evaluations in friction stir processing of commercial titanium Ti–6Al–4V. *Wear* **2013**, *302*, 1327–1333. [[CrossRef](#)]
23. Zhang, Y.; Sato, Y.S.; Kokawa, H.; Park, S.H.C.; Hirano, S. Stir zone microstructure of commercial purity titanium friction stir welded using pcBN tool. *Mater. Sci. Eng. A* **2008**, *488*, 25–30. [[CrossRef](#)]
24. Wu, L.H.; Wang, D.; Xiao, B.L.; Ma, Z.Y. Tool wear and its effect on microstructure and properties of friction stir processed Ti–6Al–4V. *Mater. Chem. Phys.* **2014**, *146*, 512–522. [[CrossRef](#)]
25. Mironov, S.; Sato, Y.S.; Kokawa, H. Friction-stir welding and processing of Ti-6Al-4V titanium alloy: A review. *J. Mater. Sci. Technol.* **2018**, *34*, 58–72. [[CrossRef](#)]
26. Gurianov, D.A.; Fortuna, S.V.; Nikonov, S.Y.; Moskvichev, E.N.; Kolubaev, E.A. Heat Input Effect on the Structure of ZhS6U Alloy. *Russ. Phys. J.* **2021**, *64*, 1415–1421. [[CrossRef](#)]
27. Zykova, A.; Vorontsov, A.; Chumaevskii, A.; Gurianov, D.; Gusarova, A.; Kolubaev, E.; Tarasov, S. Structural evolution of contact parts of the friction stir processing heat-resistant nickel alloy tool used for multi-pass processing of Ti6Al4V/ (Cu+Al) system. *Wear* **2022**, *488*, 204138. [[CrossRef](#)]
28. Amirov, A.I.; Eliseev, A.A.; Rubtsov, V.E.; Utyaganova, V.R. Butt friction stir welding of commercially pure titanium by the tool from a heat-resistant nickel alloy. *AIP Conf. Proc.* **2019**, *2167*, 020016. [[CrossRef](#)]
29. Amirov, A.I.; Eliseev, A.A.; Beloborodov, V.A.; Chumaevskii, A.V.; Gurianov, D.A. Formation of α' titanium welds by friction stir welding. *J. Phys. Conf. Ser.* **2020**, *1611*, 012001. [[CrossRef](#)]
30. Amirov, A.; Eliseev, A.; Kolubaev, E.; Filippov, A.; Rubtsov, V. Wear of ZhS6U nickel superalloy tool in friction stir processing on commercially pure titanium. *Metals* **2020**, *10*, 799. [[CrossRef](#)]
31. Amirov, A.I.; Chumaevskii, A.V.; Vorontsov, A.V. Formation of ($\alpha + \beta$) titanium welds by friction stir welding using heat-resistant alloy tool. *AIP Conf. Proc.* **2020**, *2310*, 020017. [[CrossRef](#)]
32. Balla, V.K.; Soderlind, J.; Bose, S.; Bandyopadhyay, A. Microstructure, mechanical and wear properties of laser surface melted Ti6Al4V alloy. *J. Mech. Behav. Biomed. Mater.* **2014**, *32*, 335–344. [[CrossRef](#)]
33. Mironov, S.; Sato, Y.S.; Kokawa, H. Grain structure evolution during friction-stir welding. *Phys. Mesomech.* **2020**, *23*, 21–31. [[CrossRef](#)]
34. Liu, H.J.; Zhou, L. Microstructural zones and tensile characteristics of friction stir welded joint of TC4 titanium alloy. *Trans. Nonferr. Met. Soc. China* **2010**, *20*, 1873–1878. [[CrossRef](#)]
35. Lippold, J.C.; Livingston, J.J. Microstructure evolution during friction stir processing and hot torsion simulation of Ti–6Al–4V. *Metall. Mater. Trans. A* **2013**, *44*, 3815–3825. [[CrossRef](#)]
36. Edwards, P.; Ramulu, M. Fracture toughness and fatigue crack growth in Ti–6Al–4V friction stir welds. *J. Mater. Eng. Perform.* **2015**, *24*, 3263–3270. [[CrossRef](#)]
37. Zhou, L.; Liu, H.J.; Liu, Q.W. Effect of rotation speed on microstructure and mechanical properties of Ti–6Al–4V friction stir welded joints. *Mater. Des.* **2010**, *31*, 2631–2636. [[CrossRef](#)]
38. Ji, S.; Li, Z.; Wang, Y.; Ma, L. Joint formation and mechanical properties of back heating assisted friction stir welded Ti–6Al–4V alloy. *Mater. Des.* **2017**, *113*, 37–46. [[CrossRef](#)]
39. Fall, A.; Fesharaki, M.H.; Khodabandeh, A.R.; Jahazi, M. Tool wear characteristics and effect on microstructure in Ti–6Al–4V friction stir welded joints. *Metals* **2016**, *6*, 275. [[CrossRef](#)]
40. Zykova, A.P.; Vorontsov, A.V.; Chumaevskii, A.V.; Gurianov, D.A.; Gusarova, A.V.; Savchenko, N.L.; Kolubaev, E.A. The Influence of Multipass Friction Stir Processing on Formation of Microstructure and Mechanical Properties of VT6 Alloy. *Russ. J. Non-Ferr. Met.* **2022**, *63*, 167–176. [[CrossRef](#)]